Nano Research

Open Access

Research Article

Mitigating over-oxidation and optimizing electronic structure of ruthenium sites by binary Ni-Mo_2N support for enhanced oxygen evolution reaction

Meishu Xin, Aiping Wu, Dongxu Wang, Youming Dong, Yuying Fan, Xianyun Yue, Chungui Tian ✉, and Honggang Fu ✉

Key Laboratory of Functional Inorganic Material Chemistry, Ministry of Education of the People's Republic of China, Heilongjiang University, Harbin 150080, China

Cite this article: *Nano Research*, **2026**, *19*, 94908372. https://doi.org/10.26599/NR.2026.94908372

ABSTRACT: Ruthenium-based catalysts face significant challenges of electrochemical dissolution and slow reaction kinetics for the oxygen evolution reaction (OER). Here, we have shown the enhancement of the activity and stability of Ru doped on a binary Ni-Mo_2N support with three-dimensional (3D) filamentous network structure (Ru/Ni-Mo_2N) for OER. X-ray photoelectron spectroscopy (XPS) reveals the increase of the electron density around Ru sites by the interaction with Ni-Mo_2N. Density functional theory (DFT) calculations confirm that this interaction induces a downshift of the d-band center of Ru sites, leading to optimized adsorption energies of intermediates on Ru and enhanced OER performance. Moreover, the sacrificial behavior of Ni effectively mitigates Ru over-oxidation and dissolution, thereby enhancing OER stability. Also, the 3D filamentous network structure with abundant pores is favorable to accelerate the transfer of electrolyte. As a result, the Ru/Ni-Mo_2N requires an overpotential of 251 mV to achieve 20 mA·cm^{-2}, being 83 mV lower than that of Ru-Mo_2N. An anion exchange membrane water electrolyzer (AEMWE) (Pt/C||Ru/Ni-Mo_2N) delivers a voltage of 1.78 V at 500 mA·cm^{-2}, superior to that of the Pt/C||RuO_2 (1.97 V@500 mA·cm^{-2}), and exhibits stable operation for over 500 h. This study demonstrates the critical role of the binary support in enhancing the catalytic activity and stability of Ru-based catalysts.

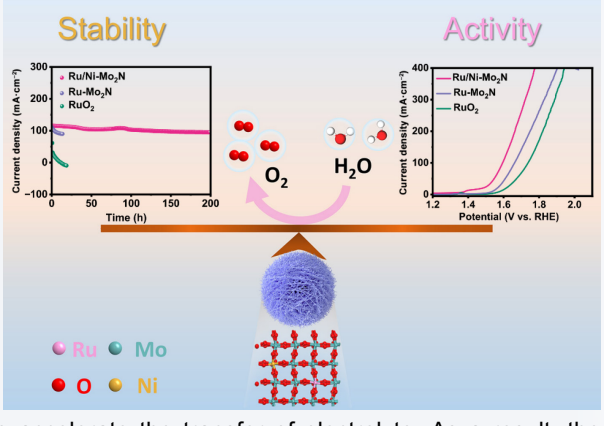

KEYWORDS: oxygen evolution reaction, Ru-based catalyst, binary support, Mo_2N, anion exchange membrane water electrolyzer (AEMWE)

1 Introduction

Electrocatalytic water splitting has emerged as a promising technology for producing green hydrogen [1–3]. Anion exchange membrane water electrolyzer (AEMWE) has attracted intensive attention for large-scale hydrogen production, as it can be coupled with renewable energy sources and operate in low alkaline system, offering both cost competitiveness and robust operational stability [4–6]. The efficiency of hydrogen production is limited by the sluggish kinetics of the oxygen evolution reaction (OER), as its complex four-electron transfer process [1, 7–9]. The development of catalysts with abundant active sites and long-term stability is essential to facilitate the reaction kinetics [10, 11]. Compared to IrO_2, Ru-based materials offer advantages for OER by their relatively higher natural abundance and lower cost [12, 13]. Nevertheless, the relatively slow transformation of reaction intermediates on Ru-based catalysts during OER process limits the development of their performance [14, 15]. Moreover, with rising OER potentials, Ru tends to undergo oxidation to form soluble high-valence species (Ru^{n+}, $n > 4$), leading to the degradation of catalysts [16, 17]. Designing low-Ru catalysts with high activity and stability in alkaline media is critically important.

Significant efforts have been devoted to developing low-Ru catalysts for OER [18, 19]. Integrating Ru with suitable supports represents an effective way for constructing effective low-Ru

Received: September 18, 2025; **Revised:** November 29, 2025
Accepted: December 24, 2025

✉Address correspondence to Chungui Tian, tianchungui@hlju.edu.cn; Honggang Fu, fuhg@vip.sina.com, fuhg@hlju.edu.cn

catalysts [20, 21]. A series of supports, including metal oxides [22, 23], nitrides [24, 25], phosphides [26, 27], and hydroxides [28, 29], have been employed to anchor Ru sites for OER. The support material plays a pivotal role in stabilizing Ru sites against agglomeration, thereby improving Ru dispersion and utilization efficiency [30–32]. Moreover, the support can modulate the d-band center of Ru, which can optimize the adsorption energy of oxygen intermediates and enhance the catalytic activity [18, 33]. For example, integrating Ru single atoms with MoO_{3-x}/nickel foam (NF) substrates effectively modulates the electronic structure of Ru, leading to enhanced intrinsic activity and accelerated OER kinetics [34]. Zhang et al. demonstrated that Ru clusters anchored on cobalt-nickel bimetallic phosphide (Ru-CoP/Ni_2P) effectively modulate the electronic structure of Ru while promoting the conversion from O* to OOH* during OER, thus significantly improving catalytic performance [35]. Niu et al. synthesized Ru-VO_2 composites with Ru-doped VO_2 and Ru nanoparticles (NPs). The sacrificial dissolution of V from VO_2 substrate inhibits the dissolution of Ru species and protects Ru NPs from over-oxidation, thereby enhancing OER stability [36]. It is promising to simultaneously achieve high OER activity and suppress over-oxidation during operation by rational structure design of support materials.

Herein, we propose an effective strategy by combining the Ru sites with a binary Ni-Mo_2N support for enhancing the activity and stability of OER. The Ru/Ni-Mo_2N has shown three-dimensional (3D) filamentous network architecture with plentiful pores, enabling full electrolyte accessibility and facilitating mass transport. The electronic structure of Ru sites is modulated by the binary Ni-Mo_2N support. Density functional theory (DFT) calculations indicate that the downshift of the d-band center at Ru sites optimizes the adsorption of oxygen intermediates, thereby enhancing the catalytic activity. Also, the sacrificial oxidation of Ni sites mitigates the over-oxidation of Ru during OER, significantly enhancing durability. Consequently, the Ru/Ni-Mo_2N requires an overpotential of only 251 mV to achieve 20 mA·cm^{-2}, superior to that of Ru-Mo_2N (334 mV@20 mA·cm^{-2}). Moreover, a two-electrode electrolyzer assembled with Ru/Ni-Mo_2N (anode) and Pt/C (cathode) demonstrates a low cell voltage of 1.483 V at 10 mA·cm^{-2}, outperforming the Pt/C||RuO_2 benchmark (1.563 V). AEMWE performance of Pt/C||Ru/Ni-Mo_2N (1.78 V@500 mA·cm^{-2}) was also superior to Pt/C||RuO_2 (1.97 V@500 mA·cm^{-2}), and it demonstrates enhanced operational stability for over 500 h at 500 mA·cm^{-2}. The study opens a promising strategy to improve activity and stability of Ru-based catalysts for OER.

2 Results and discussion

2.1 Preparation and characterization of Ru/Ni-Mo_2N

The Ru/Ni-Mo_2N catalyst with a filamentous network morphology was synthesized by annealing a RuNi-MoO_x precursor under an ammonia atmosphere, as depicted in Fig. 1(a). As is known, the reaction of Mo powder in H_2O_2 can form a $MoO_2(OH)(OOH)$ solution, which can be converted into MoO_3 under solvothermal conditions [37]. At the same time, in the presence of H_2O_2, Ru^{3+} and Ni^{2+} can form corresponding Ru-based and Ni-based materials [38, 39]. So, in our present synthesis, it is proposed that the Ru^{3+} and Ni^{2+} are combined with $MoO_2(OH)(OOH)$ to form RuNi-MoO_x precursor based mainly on the following process (Eqs. (1)–(3)). The detailed schematic structure is presented in Fig. 1(a). The RuNi-MoO_x precursor exhibits a crystalline structure consisting of $MoO_{2.80}$ (PDF#12-0517) and Mo_4O_{11} (PDF#13-0142) (Fig. S1 in the Electronic Supplementary Material (ESM)), while the MoO_3 phase (PDF#05-0508) was observed in the undoped precursor (Fig. S2 in the ESM). The presence of unsaturated molybdenum oxide species in RuNi-MoO_x is induced by inhomogeneity and disturbs the electronic structure, which is attributed to the incorporation of Ru^{3+} and Ni^{2+} [40]

$$Mo + 4H_2O_2 \rightarrow MoO_2(OH)(OOH) + 3H_2O \quad (1)$$

$$2MoO_2(OH)(OOH) \rightarrow 2MoO_3 + 2H_2O + O_2 \quad (2)$$

$$MoO_2(OH)(OOH) \xrightarrow{Ru^{3+},\ Ni^{2+}} RuNi\text{-}MoO_x + H_2O + O_2 \quad (3)$$

Scanning electron microscopy (SEM) images (Figs. 1(b) and 1(c)) reveal that the RuNi-MoO_x precursor exhibits a 3D filamentous network morphology. Transmission electron microscopy (TEM) images (Fig. 1(d) and Fig. S3 in the ESM) further confirm this architecture. The nitrogen adsorption–desorption measurement indicates that the precursor possesses a Brunauer–Emmett–Teller (BET) specific surface area (S_{BET}) of 24.06 m^2·g^{-1} (Fig. S4 in the ESM), suggesting a relatively high surface area conducive to catalytic reactions. The morphology of the catalysts is significantly influenced by the type of metal doping and the experimental parameters. In contrast to the filamentous network morphology of RuNi-MoO_x, the individual doping of Ru or Ni results in nanoparticle and nanoflower architectures, respectively (Fig. S5 in the ESM). The distinctive filamentous network of RuNi-MoO_x is attributed to the synergistic incorporation of both Ru and Ni. Furthermore, the morphology of the precursor evolves from a stacked structure composed of curved nanosheets into a filamentous network with increasing synthesis time (Fig. S6 in the ESM).

The Ru/Ni-Mo_2N catalyst was prepared by sintering the precursor at 550 °C for 2 h under an ammonia atmosphere. SEM images of Ru/Ni-Mo_2N (Figs. 1(e) and 1(f)) show that the 3D filamentous network structure is well maintained after nitridation. TEM analysis (Figs. 1(g) and 1(h)) further confirms that the catalyst possesses a 3D filamentary network architecture and there are a large number of pores present on the nanostructures, which is beneficial for exposing more edge active sites. The high-resolution TEM (HRTEM) images (Figs. 1(i) and 1(j)) reveal two distinct lattice fringes with measured spacings of 0.227 and 0.209 nm, corresponding to the (111) and (200) planes of Mo_2N, respectively. Furthermore, the interplanar spacing of the (111) plane in Ru/Ni-Mo_2N is measured to be 0.227 nm, indicating a noticeable contraction compared to that of pure Mo_2N (0.240 nm) (Fig. S7 in the ESM). This contraction is attributed to the substitution of Mo atoms by Ru and Ni within the Mo_2N lattice, which induces lattice distortion and consequently contracts the interplanar spacings. The elemental mapping (Fig. 1(k)) exhibits that the elements Ru, Ni, Mo, and N are uniformly dispersed throughout the framework structure and no agglomerations exist. Furthermore, energy-dispersive X-ray spectroscopy (EDS) analysis confirms the successful incorporation of Ru and Ni into the Mo_2N framework, as quantified by the elemental mass ratios provided in Fig. S8 in the ESM. Collectively, these characterization data confirm the successful synthesis of the Ru/Ni-Mo_2N composite. This structure exhibits superior capillary forces, which facilitate efficient electrolyte

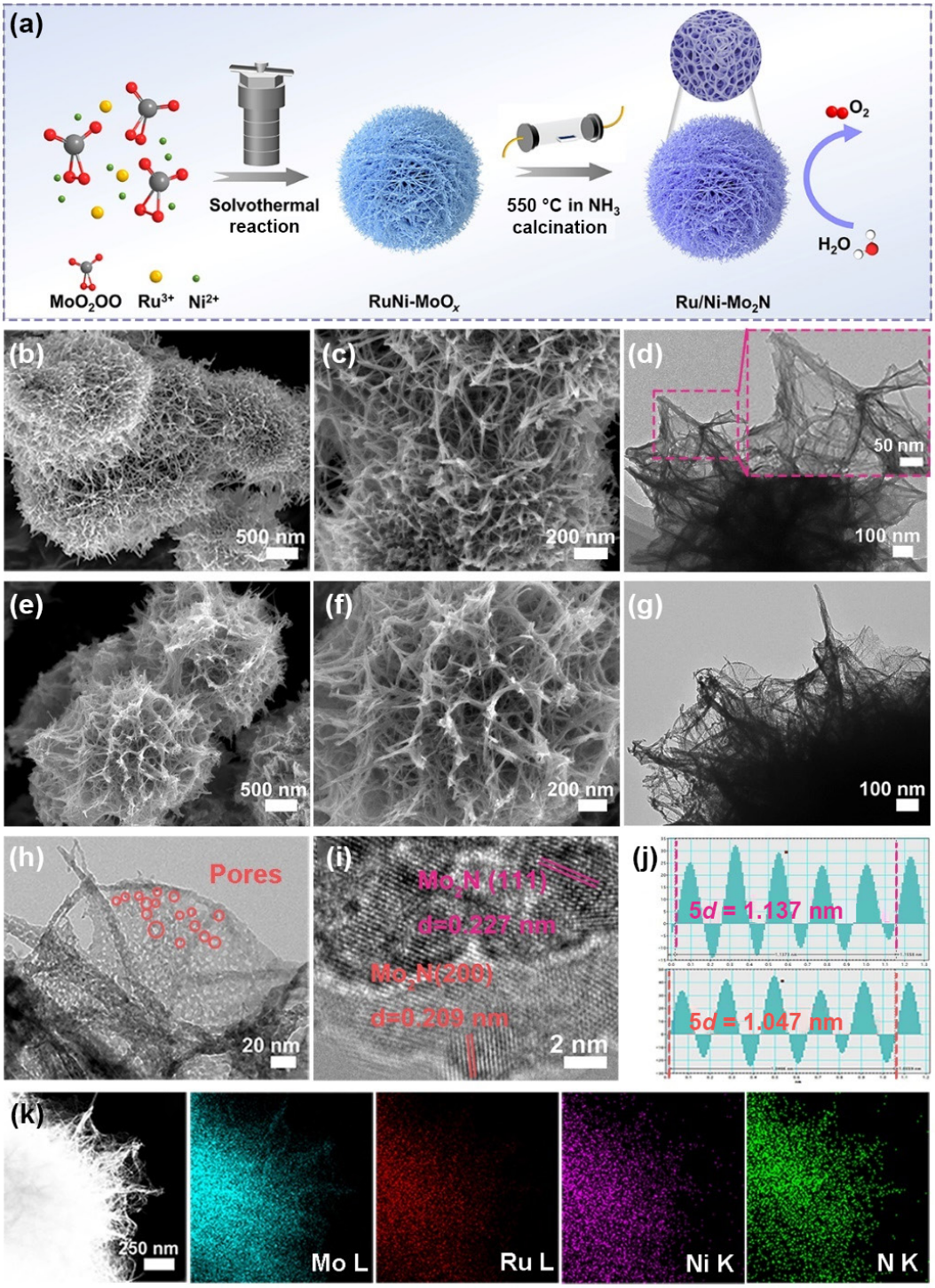

Figure 1 (a) Schematic process for the synthesis of Ru/Ni-Mo_2N. ((b) and (c)) SEM images of RuNi-MoO_x. (d) TEM image of RuNi-MoO_x. ((e) and (f)) SEM images, ((g) and (h)) TEM images, ((i) and (j)) HRTEM images, and (k) scanning TEM (STEM) and EDS elemental mappings of Ru/Ni-Mo_2N.

penetration and synergistically enhance the electrode–electrolyte interfacial interaction [41]. Nitrogen adsorption–desorption measurements (Fig. 2(a)) indicate that Ru/Ni-Mo_2N and Ru-Mo_2N exhibit specific surface areas of 30.23 and 9.75 $m^2 \cdot g^{-1}$, respectively. Compared to Ru-Mo_2N, Ru/Ni-Mo_2N possesses a higher specific surface area and greater pore volume, which facilitates the exposure of more active sites. From the contact angle measurement, Ru/Ni-Mo_2N showed an excellent wettability to alkaline electrolyte (Fig. S9 in the ESM), which can be attributed to its unique morphology. The metal content in the prepared catalyst was confirmed by inductively coupled plasma optical emission spectroscopy (ICP-OES). The ICP-OES tests show that the Mo, Ni, and Ru contents in the catalyst were 80.5 wt.%, 3.0 wt.%, and 1.2 wt.%, respectively (Table S2 in the ESM). The detectable presence of Ru and Ni confirms their successful incorporation into the catalyst.

X-ray diffraction (XRD) patterns (Figs. 2(b) and 2(c)) show that the diffraction peaks of the Ru/Ni-Mo_2N catalyst match those of phase-pure Mo_2N (PDF#25-1366). The diffraction peaks located at

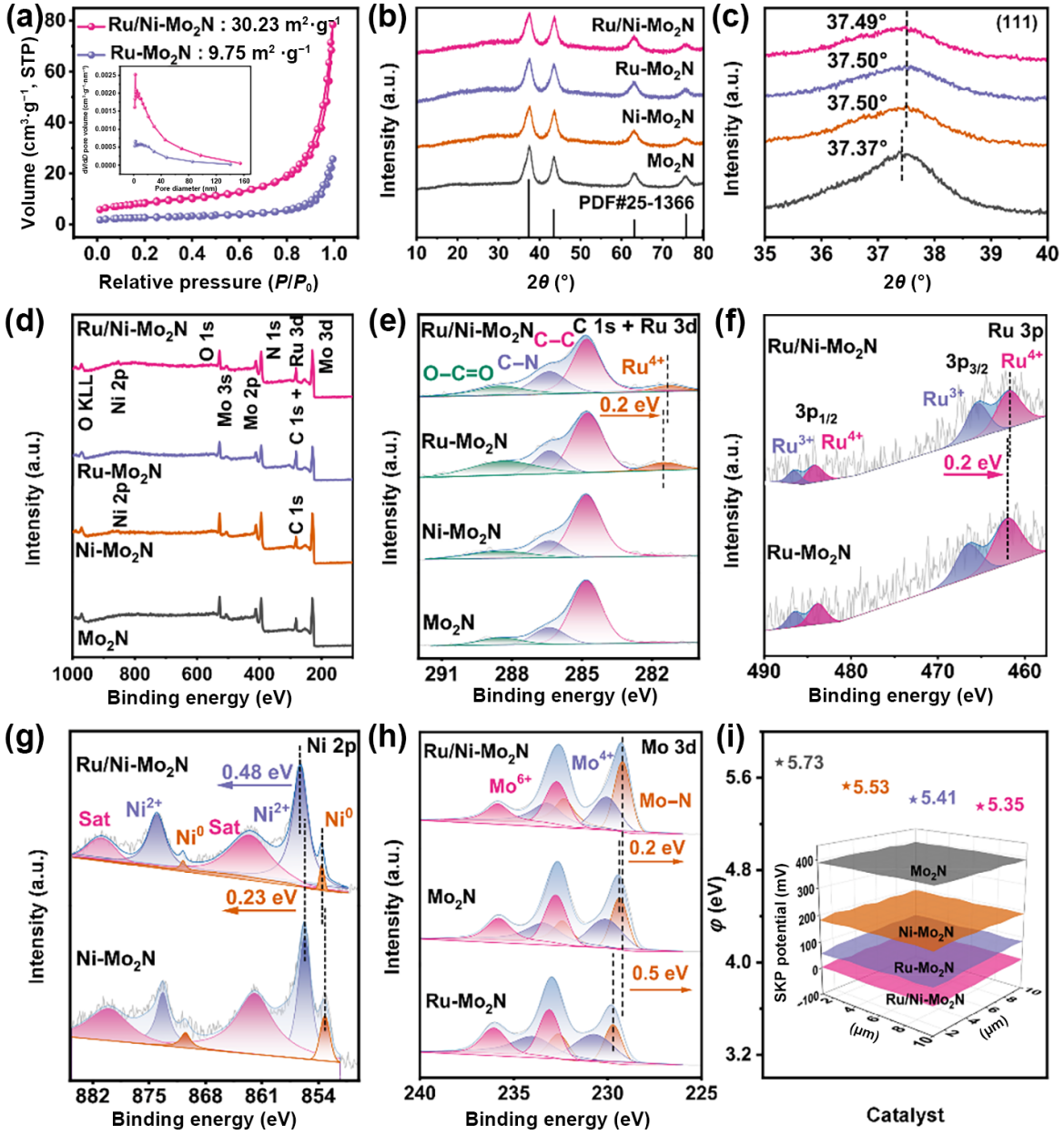

Figure 2 (a) BET for Ru/Ni-Mo_2N and Ru-Mo_2N. ((b) and (c)) XRD patterns of Ru/Ni-Mo_2N, Ru-Mo_2N, Ni-Mo_2N and Mo_2N. (d) The full XPS survey spectra of Ru/Ni-Mo_2N, Ru-Mo_2N, Ni-Mo_2N, and Mo_2N. (e) C 1s + Ru 3d of Ru/Ni-Mo_2N, Ru-Mo_2N, Ni-Mo_2N, and Mo_2N. (f) Ru 3p of Ru/Ni-Mo_2N and Ru-Mo_2N. (g) Ni 2p of Ru/Ni-Mo_2N and Ni-Mo_2N. (h) Mo 3d of Ru/Ni-Mo_2N, Ru-Mo_2N, and Mo_2N. (i) SKP of Ru/Ni-Mo_2N, Ru-Mo_2N, Ni-Mo_2N, and Mo_2N.

37.2°, 43.5°, 62.8°, and 75.5° can be assigned to the (111), (200), (220), and (311) planes of Mo_2N, respectively. Notably, the (111) diffraction peak of Ru/Ni-Mo_2N shifts slightly to a higher angle (37.49°) compared to that of pure Mo_2N, indicating lattice contraction along the (111) plane due to the incorporation of Ru and Ni atoms with smaller atomic radii. This finding is consistent with the lattice contraction observed by HRTEM. This shift is also observed in the XRD patterns of Ru-Mo_2N and Ni-Mo_2N samples when either Ru or Ni is individually introduced, further supporting the successful doping of both elements into the Mo_2N lattice. Furthermore, the XRD pattern of Ru/Ni-Mo_2N exhibits only diffraction peaks corresponding to Mo_2N, indicating that the doping process did not alter the host crystal structure. The absence of separate Ru or Ni phases also confirms the low concentration and homogeneous dispersion of the dopants within the catalyst.

The surface chemical composition was analyzed using X-ray photoelectron spectroscopy (XPS). In contrast to Ru-Mo_2N, Ni-Mo_2N, and Mo_2N, the full XPS survey spectrum of Ru/Ni-Mo_2N (Fig. 2(d)) exhibits characteristic peaks of Ni 2p and Ru 3d + C 1s at binding energies of 854.1 and 284.8 eV, respectively [4], confirming the successful incorporation of Ru and Ni into the catalyst. The high-resolution XPS spectra of Ru 3d + C 1s are presented in Fig. 2(e). In contrast to Ni-Mo_2N and Mo_2N, distinct peaks corresponding to Ru^{4+} $3d_{5/2}$ are clearly observed in both Ru/Ni-Mo_2N and Ru-Mo_2N. As shown in Fig. 2(f), the Ru 3p peaks of the Ru/Ni-Mo_2N catalyst are observed at binding energies of 461.8 and 484.0 eV, corresponding to Ru^{4+} $3p_{3/2}$ and $3p_{1/2}$, respectively [42, 43]. Compared to RuO_2, the Ru^{4+} peak in Ru/Ni-Mo_2N shows a negative binding energy shift (Fig. S10(a) in the ESM), indicating a valence state below +4 [43, 44]. Moreover, compared to Ru-Mo_2N, both the

Ru 3d and Ru 3p peaks of Ru/Ni-Mo_2N shift toward lower binding energies, suggesting the incorporation of Ni promotes electron transfer to Ru. Furthermore, catalysts with elevated Ru loading (3%) were synthesized to verify the electronic modulation effect of the binary support on Ru sites. Consistently, the introduction of Ni into the support enhances the electron density at Ru centers (Fig. S10(b) in the ESM). This electronic modulation helps suppress the over-oxidation of Ru, significantly enhancing the catalytic stability of the material [45]. The Ni 2p XPS spectra (Fig. 2(g)) show peaks at 853.5 and 870.8 eV, which are assigned to metallic Ni^0, along with additional peaks at 856.2 and 874.0 eV corresponding to Ni^{2+} $2p_{3/2}$ and Ni^{2+} $2p_{1/2}$, respectively [46, 47]. The presence of Ni^{2+} species is attributed to surface oxidation resulting from air exposure. In Ru/Ni-Mo_2N, the Ni 2p peaks shift positively by +0.23 eV for Ni^0 and +0.48 eV for Ni^{2+} compared to those in Ni-Mo_2N, indicating electron withdrawal from Ni sites. The Mo 3d spectrum of Ru/Ni-Mo_2N (Fig. 2(h)) is deconvoluted into three doublets: Mo–N (229.4 and 232.4 eV), Mo^{4+} (230.1 and 233.4 eV), and Mo^{6+} (232.7 and 235.8 eV) [48]. The presence of Mo^{4+} and Mo^{6+} species is likely due to surface oxidation upon air exposure. A comparative analysis between Ru/Ni-Mo_2N and Mo_2N indicates that doping with Ru and Ni induces a negative binding energy shift of the Mo–N bond, suggesting electron acquisition by Mo. Further comparison between Ru/Ni-Mo_2N and Ru-Mo_2N reveals an additional negative shift in the Mo–N binding energy, implying that Ni incorporation promotes further electron enrichment at Mo sites. Together with previous findings, these results demonstrate that introducing Ni leads to increased electron density at both Mo and Ru sites in the catalyst. This electronic modulation contributes to enhanced structural stability during the OER process [45]. The scanning Kelvin probe (SKP) measurements (Fig. 2(i)) show that the binary Ni-Mo_2N support modified Ru catalyst (Ru/Ni-Mo_2N) has the lowest work function among the series, indicating facilitated electron transfer from the catalyst bulk to the surface. This enhanced electron exchange capability with the electrolyte improves the reaction kinetics [49, 50].

2.2 Water oxidation performance in alkaline

The OER performance of Ru/Ni-Mo_2N was evaluated in a 1.0 M KOH electrolyte using a standard three-electrode system. The electrolyte was saturated with N_2 prior to measurements. The prepared NF coated with the catalysts was used as the working electrode, while the graphite rod and a Hg/HgO electrode were used as the counter and reference electrode, respectively. Both Ru and Ni play crucial roles during the synthesis, and their content significantly governs the catalytic performance. To investigate the effects, a series of comparative samples with varying Ru and Ni loadings was synthesized. As shown in Fig. S11 in the ESM, the Ru/Ni-Mo_2N catalyst with Ru and Ni loading of 1% and 4% (relative to Mo) exhibited optimal OER performance. This result can be attributed to the optimal Ru/Ni ratio, which effectively modulates the electronic structure of Ru while enabling Ni to properly suppress its over-oxidation. As shown in Fig. 3(a), Ru/Ni-Mo_2N exhibits an overpotential of 251 mV at a current density of 20 $mA{\cdot}cm^{-2}$, which is lower than those of Ru-Mo_2N (334 mV), Ni-Mo_2N (393 mV), Mo_2N (432 mV), and commercial RuO_2 (384 mV). The results indicate that the metallic composition significantly influences the catalyst's performance, with Ru serving as the primary active site compared to Ni. The higher overpotentials observed for Ru/Ni-Mo_2N-6h (338 mV), Ru/Ni-Mo_2N-450 (320 mV), and Ru/Ni-Mo_2N-650 (300 mV) relative to Ru/Ni-Mo_2N (Figs. S12 and S13 in the ESM) demonstrate the additional influence of morphological and crystallographic properties on catalytic performance. To account for Ohmic resistance, the linear scanning voltammetry (LSV) curves with 90% *iR* compensation (Figs. S14(a) and S14(b) in the ESM) are provided. The results show that Ru/Ni-Mo_2N requires overpotentials of only 265 and 316 mV to achieve current densities of 20 and 100 $mA{\cdot}cm^{-2}$, respectively, underscoring its outstanding catalytic activity, especially at high current densities. To minimize interference from redox features, reverse-scan measurements were also conducted (Figs. S14(c) and S14(d) in the ESM). Even under reverse scanning conditions, Ru/Ni-Mo_2N still exhibits the lowest overpotentials, further corroborating its exceptional OER performance.

Furthermore, the catalytic reaction kinetics were evaluated using the Tafel slope. The Ru/Ni-Mo_2N catalyst demonstrates the most favorable reaction kinetics, exhibiting the smallest Tafel slope of 53 $mV{\cdot}dec^{-1}$, which is significantly lower than those of Ru-Mo_2N (90 $mV{\cdot}dec^{-1}$), Ni-Mo_2N (136 $mV{\cdot}dec^{-1}$), Mo_2N (282 $mV{\cdot}dec^{-1}$), and RuO_2 (94 $mV{\cdot}dec^{-1}$) (Fig. 3(b)). The excellent OER activity of Ru/Ni-Mo_2N can be attributed to its unique 3D filamentous network morphology and the electronic modulation of Ru sites by the binary Ni-Mo_2N support, distinguishing it from other comparative samples. The 3D filamentous network structure offers abundant exposed active sites and promotes electrolyte penetration and mass transport, as supported by its superior wettability indicated by the small contact angle (Fig. S9 in the ESM) [6]. Turnover frequency (TOF) values were calculated to evaluate the intrinsic activity per active site. As shown in Fig. 3(c) and Fig. S15 in the ESM, Ru/Ni-Mo_2N achieves a TOF value of 0.202 s^{-1} at 1.50 V vs. reversible hydrogen electrode (RHE), which is higher than those of Ru-Mo_2N (0.061 s^{-1}) and RuO_2 (0.036 s^{-1}), indicating superior catalytic efficiency. Mass activity measurements further corroborated these findings, with Ru/Ni-Mo_2N exhibiting a mass activity of 359.3 $A{\cdot}g_{Ru}^{-1}$ at 1.5 V vs. RHE, significantly exceeding those of Ru-Mo_2N (73.2 $A{\cdot}g_{Ru}^{-1}$) and RuO_2 (1.6 $A{\cdot}g_{Ru}^{-1}$) (Fig. 3(c) and Fig. S16 in the ESM). These results highlight that electronic modulation of the Ru site by Ni-Mo_2N support engineering enhances conductivity and intrinsic activity. Electrochemical active surface area (ECSA) is used to evaluate the density of catalysts exposing active sites, which was evaluated by the double layer capacitance (C_{dl}). The results show that the calculated ECSA of Ru/Ni-Mo_2N (1640 cm^2) is larger than that of Ru-Mo_2N (860 cm^2) (Fig. 3(d) and Figs. S17 and S18 in the ESM), indicating a higher density of accessible active sites. This enhancement is likely due to improved electron transfer within the catalyst framework.

Next, electrochemical impedance spectroscopy (EIS) tests were performed to study the electrode kinetics. The EIS data is fitted to a semicircle, and the diameter of the semicircle is consistent with the charge transfer resistance (R_{ct}) of the catalyst. A smaller R_{ct} implies a higher charge transfer rate and faster catalytic kinetics. EIS measurements show the smallest R_{ct} for Ru/Ni-Mo_2N (Fig. S19 in the ESM), consistent with its accelerated reaction kinetics. A radar chart (Fig. 3(e)) comprehensively compares the OER performance metrics, including overpotentials at 20 and 100 $mA{\cdot}cm^{-2}$, Tafel slope, R_{ct}, and C_{dl}, highlighting the overall advantage of Ru/Ni-Mo_2N over other samples. In addition to high activity, the catalyst also exhibited remarkable stability. After 4000 cyclic voltammetry (CV) cycles, the polarization curve of Ru/Ni-Mo_2N demonstrates

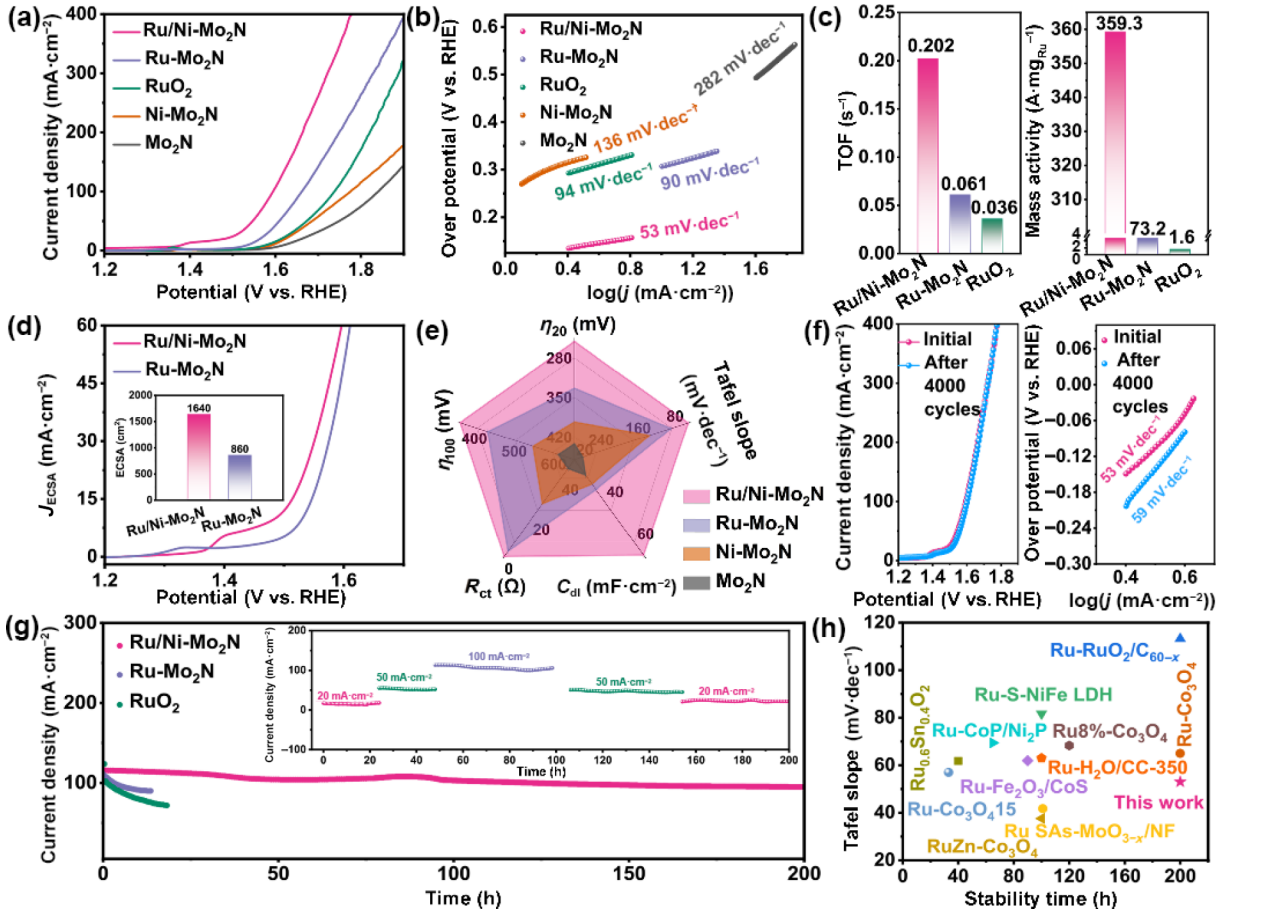

Figure 3 (a) LSV curves and (b) Tafel slopes of Ru/Ni-Mo_2N, Ru-Mo_2N, Ni-Mo_2N, Mo_2N, and RuO_2. (c) TOF and mass activity of Ru/Ni-Mo_2N, Ru-Mo_2N, and RuO_2. (d) ECSA of Ru/Ni-Mo_2N and Ru-Mo_2N. (e) Relevant OER performance comparison radar chart. (f) Polarization curves and Tafel slopes for Ru/Ni-Mo_2N before and after 4000 cycles of CV test. (g) The time dependence of the catalytic current during electrolysis over the course of 200 h in 1.0 M KOH. (h) Comparison of Tafel slope and stability time for OER with the reported Ru-based electrocatalyst.

nearly complete overlap with the initial curve (Fig. 3(f)), and the Tafel slope remained virtually unchanged, demonstrating exceptional electrochemical stability. More importantly, the catalyst exhibits excellent long-term stability, maintaining performance for over 200 h at 100 mA·cm^{-2} in 1.0 M KOH (Fig. 3(g)). Compared to Ru-Mo_2N and RuO_2, Ru/Ni-Mo_2N demonstrates significantly improved long-term stability, indicating that the binary Ni-Mo_2N support effectively stabilizes the Ru species and its OER activity. In addition, the fluctuations in the current profile of Ru/Ni-Mo_2N were negligible after 200 h of continuous operation of the catalyst at 20, 50, and 100 mA·cm^{-2} (inset, Fig. 3(g)), indicating robust structural and catalytic integrity. Additionally, the stability of Ni-Mo_2N was evaluated (Fig. S20 in the ESM), with the results demonstrating that Ru serves as the primary active species during the stability test. The Tafel slope value and long-lasting stability of Ru/Ni-Mo_2N surpass those of most reported Ru-based electrocatalysts (Fig. 3(h) and Table S4 in the ESM). The above results indicate that the Ru supported by binary Ni-Mo_2N support exhibits excellent activity and stability in alkaline OER process.

To explore the kinetics of the OER process and the charge transfer process, *in-situ* EIS measurements were carried out at various voltages. Bode plots of Ru/Ni-Mo_2N and Ru-Mo_2N are compared in Figs. 4(a) and 4(b). Both catalysts show two distinct peaks in the Bode plots, corresponding to different processes. The peaks in the low-frequency (0.01–100 Hz) and high-frequency (100–100,000 Hz) regions are attributed to charge transfer reactions at the electrolyte–catalyst interface and electron conduction within the catalyst bulk, respectively. In the high-frequency range, Ru/Ni-Mo_2N and Ru-Mo_2N exhibit similar phase angles, suggesting comparable intrinsic electron transport resistance. In contrast, Ru/Ni-Mo_2N shows a smaller phase angle in the low-frequency region, indicating reduced interfacial charge transfer resistance. This implies that the binary support enhances the interfacial interaction between the catalyst and the electrolyte, thereby facilitating charge transfer and improving OER activity. Moreover, the phase angle of Ru/Ni-Mo_2N decreases more rapidly with increasing potential than that of Ru-Mo_2N (Fig. 4(c)), demonstrating superior electron conduction due to an optimized internal electron transport pathway. The Nyquist plots (Figs. S21(a)–S21(c) in the ESM) were fitted using an equivalent circuit model consisting of three components: electrolyte resistance (R_s), a parallel constant phase element and resistance (CPE_1 and R_{CEOR}, where R_{CEOR} is the resistance of catalyst electrochemical oxidization reaction) associated with electron transport from the bulk to the interface (reflecting surface reconstruction during OER), and another parallel element (CPE_2 and R_{OER}, where R_{OER} is the resistance of oxygen evolution reaction) related to the interfacial OER process. Notably, Ru/Ni-Mo_2N exhibits a lower R_{CEOR} value (Fig. S21(d) in the ESM), confirming enhanced catalyst–electrolyte interaction and improved charge transfer. Furthermore, in the low-

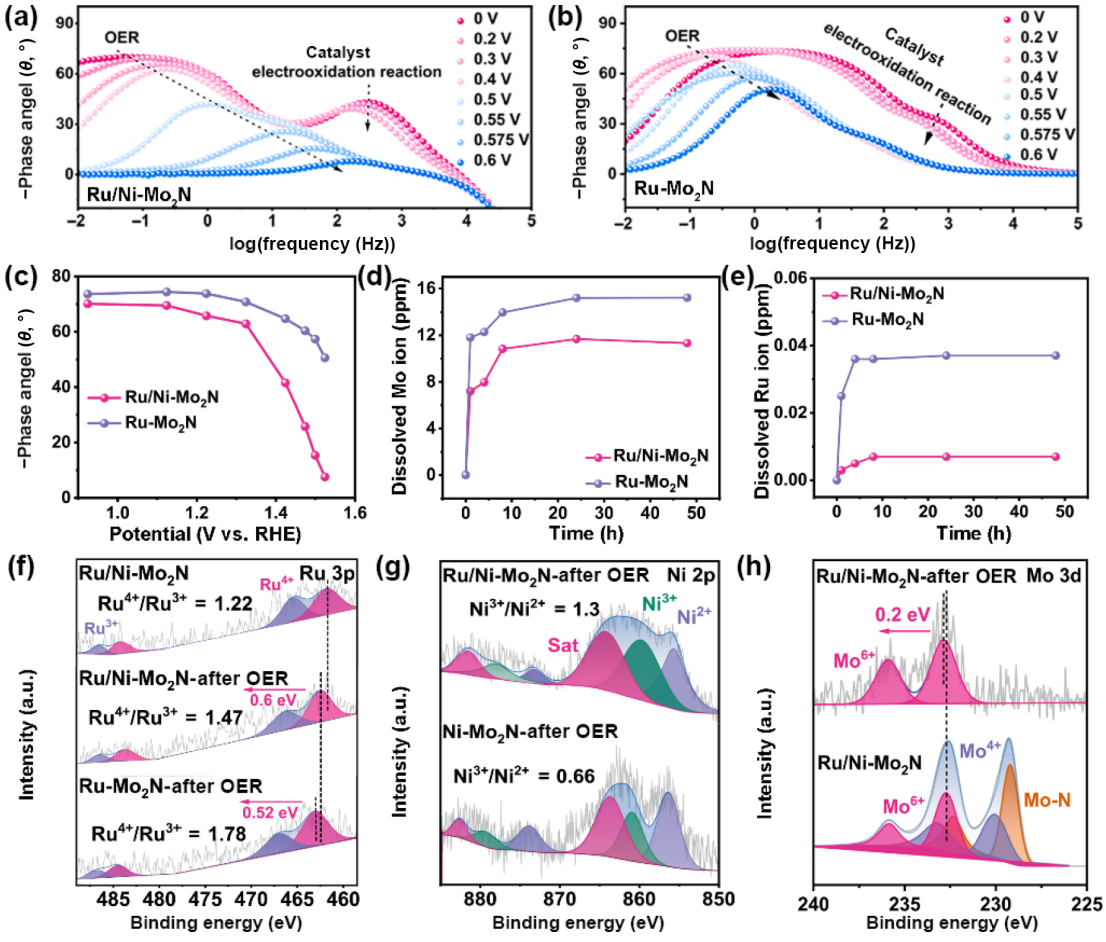

Figure 4 *In-situ* Bode phase angle plots for (a) Ru/Ni-Mo_2N and (b) Ru-Mo_2N. (c) Response of the phase angle to the applied potential of Ru/Ni-Mo_2N and Ru-Mo_2N. Dissolved (d) Mo ion and (e) Ru ion concentrations measured for Ru/Ni-Mo_2N and Ru-Mo_2N in the electrolyte by ICP-OES. (f) Ru 3p of Ru/Ni-Mo_2N (pristine), Ru/Ni-Mo_2N-after OER, and Ru-Mo_2N-after OER. (g) Ni 2p of Ru/Ni-Mo_2N-after OER and Ni-Mo_2N-after OER. (h) Mo 3d of Ru/Ni-Mo_2N (pristine) and Ru/Ni-Mo_2N-after OER.

potential range (0.924–1.424 V), the R_{OER} of Ru/Ni-Mo_2N decreases sharply and approaches zero above 1.424 V, indicating early initiation of OER. In contrast, Ru-Mo_2N requires a higher overpotential (> 1.499 V) to achieve a similar reduction in R_{OER} (Fig. S21(e) in the ESM). These results highlight that the Ru supported by binary Ni-Mo_2N support enhances charge transfer, thereby significantly lowering the reaction energy barrier.

2.3 Mechanism analysis

The ICP-OES was used during the stability tests to monitor the temporal evolution of metal concentration in the electrolyte. The results of Ru/Ni-Mo_2N indicate that Mo and Ru leached rapidly into the solution during the initial stage of the reaction, with their concentrations stabilizing after approximately 8 h. In contrast, no detectable leaching of Ni was observed throughout the entire process. The dissolution of Mo is attributed to the oxidation of Mo_2N, forming soluble molybdate ions (MoO_4^{2-}), while Ru dissolution results from partial over-oxidation under OER conditions. During the OER process, Mo_2N can leach in the form of MoO_4^{2-} ions, driven by the combined effects of KOH etching and potential-induced oxidation [51]. After 8 h of operation, a dynamic equilibrium between the leaching and redeposition of MoO_4^{2-} is established (Fig. 4(d)), contributing to improved catalytic stability [52, 53]. The XRD pattern shows no significant changes in the peak intensity of the Mo_2N phase (Fig. S22 in the ESM). The minimal dissolution of Ru indicates that the leaching of Mo has negligible impact on the stability of Ru species. Notably, MoO_4^{2-} promotes charge transfer and optimizes the electronic structure, thereby enhancing OER kinetics [51, 54]. Compared to Ru-Mo_2N, employing binary Ni-Mo_2N support significantly mitigates the electrochemical dissolution of Mo in Ru/Ni-Mo_2N during the OER. Notably, the dissolution of Ru is also markedly suppressed in Ru/Ni-Mo_2N relative to Ru-Mo_2N (Fig. 4(e)), revealing that Ni doping effectively suppresses the dissolution of Ru during electrocatalysis.

To gain deeper insight into the oxidative evolution of the catalyst during OER, we conducted XPS analysis on after-OER samples. The Ru 3p XPS spectrum of Ru/Ni-Mo_2N-after OER (Fig. 4(f)) exhibits slight positive binding energy shifts for both Ru^{4+} and Ru^{3+} species, indicating an altered electronic environment following electrochemical testing. The Ru^{4+}/Ru^{3+} ratio increased from 1.22 (pre-OER) to 1.47 (after-OER), suggesting partial oxidation of Ru^{4+} to higher-valence Ru^{n+} ($n > 4$), consistent with Ref. [8]. In addition, Ru-Mo_2N-after OER shows a more pronounced positive shift in the Ru^{4+} peak and a higher Ru^{4+}/Ru^{3+} ratio (1.78), implying that Ni incorporation moderates the over-oxidation of Ru. However, the Ni 2p XPS spectra (Fig. 4(g) and Fig. S23 in the ESM) reveal a significantly higher Ni^{3+}/Ni^{2+} ratio in Ru/Ni-Mo_2N-after OER compared to Ni-Mo_2N-after OER, indicating that Ni species in

Ru/Ni-Mo_2N are more susceptible to oxidation compared to those in Ni-Mo_2N. This phenomenon reveals that Ni may have played a self-sacrificing role in the OER process. This finding is consistent with the metal dissolution results observed during the stability test shown in Fig. 4(e). Meanwhile, the Mo 3d spectra (Fig. 4(h)) show complete disappearance of Mo–N bonds and predominant formation of Mo^{6+} species, confirming extensive oxidation of Mo to high-valence MoO_x during OER operation. The O 1s XPS spectra show a −0.60 eV shift for the O–M bond (Fig. S24 in the ESM), suggesting enhanced metal-oxygen charge transfer that increases interfacial electron density and facilitates OER kinetics [55]. The corresponding oxidation signals were detected by XPS, indicating that the dissolution is confined to the catalyst surface. Raman spectroscopy (Fig. S25(a) in the ESM) confirms the structural evolution, with peaks for Ru–O, Ni–O, and Mo–O vibrations confirming the formation of a reconstituted Ru/Ni-MoO_x surface after OER [56, 57]. Combined Raman and XPS analyses confirm the formation of a Ru/Ni-MoO_x structure following OER operation.

During the OER process, the Ru/Ni-Mo_2N catalyst undergoes partial dissolution of Mo and Ru species, along with oxidation of the Ni component. This oxidative reconstruction behavior likely facilitates the formation of the active phases. To monitor the structural and chemical evolution, we employed XRD, SEM, and TEM to characterize the after-OER catalyst (denoted as Ru/Ni-Mo_2N-after OER). The XRD pattern (Fig. S22 in the ESM) confirms that all diffraction peaks match well with the standard pattern of Mo_2N (PDF#25-1366). SEM and TEM images (Figs. S25(b)–S25(f) in the ESM) show that the catalyst retains its 3D filamentous network morphology after OER. Additionally, a distinct amorphous layer is observed on the surface, suggesting partial reconstruction into an active MoO_x phase, which has been reported to enhance the OER activity of Ru sites [58]. Elemental mapping and EDS by TEM (Figs. S25(g) and S26 in the ESM) reveal a homogeneous distribution of Ru, Mo, Ni, and O without noticeable agglomeration. A significant increase in oxygen content is observed, consistent with extensive surface oxidation during OER. These results collectively demonstrate that the Ru/Ni-Mo_2N catalyst maintains its fundamental crystal structure and morphological integrity after alkaline OER, underscoring its robust structural stability.

To further investigate the OER pathways, the oxygen intermediate species generated on the electrocatalysts during OER were identified using *in-situ* infrared (IR) analysis. Figure 5(a) displays the potential-dependent *in-situ* IR spectra of Ru/Ni-Mo_2N, recorded by stepping the potential from the open circuit potential (OCP) to 1.8 V. A distinct absorption band emerges at 1121 cm^{-1} [59], which is attributed to the *OOH intermediate. Similar spectral changes were also observed on Ru-Mo_2N (Fig. 5(b)), indicating that the OER on both catalysts proceeds primarily via the adsorbate evolution mechanism (AEM). The stronger peak also indicates an increase in *OOH formation, suggesting a reduction in the reaction energy barrier (*O + H_2O → *OOH + H^+ + e^-). Furthermore, we use tetramethylammonium cation (TMA^+) to detect O_2^{2-} species produced from lattice oxygen mechanism (LOM) based on strong electrostatic interaction. Ru/Ni-Mo_2N shows only minor attenuation of OER activity in 1.0 M TMAOH compared to 1.0 M KOH (Fig. S27 in the ESM), supporting the conclusion that the AEM is the dominant pathway, consistent with the *in-situ* IR results.

2.4 DFT calculations

Based on above analyses, the enhanced activity and stability of Ru/Ni-Mo_2N should be ascribed to following points. (1) The binary support Ni-Mo_2N modulates the electronic structure of Ru, leading to an enriched electron density at the Ru sites. (2) The sacrificial behavior of Ni effectively mitigates Ru over-oxidation and dissolution, thereby enhancing OER stability. (3) The leaching of MoO_4^{2-} into the electrolyte facilitates charge transfer and optimizes the electronic structure, thereby improving the overall catalytic performance. Also, the 3D filamentous network structure with abundant pores is favorable to accelerate the transfer of electrolyte. We have performed the DFT calculations to further elucidate these phenomena.

DFT calculations were performed to clarify the effect of Ru supported by the binary catalyst on the modified OER performance of Ru/Ni-MoO_x. Combined with XPS analysis and Refs. [60–62], it is demonstrated that the surface-reconstructed MoO_x significantly enhances the OER activity. Based on the above analysis, we constructed models of Ru supported on binary Ni-MoO_x (Ru/Ni-MoO_x) and monometallic MoO_x (Ru-MoO_x) (Fig. 5(c)). The OER mechanism typically involves four proton–electron transfer steps and three successive intermediates (*OH, *O, and *OOH, where the asterisk denotes the adsorption site). Initially, we calculated the adsorption free energy of the key intermediates on Ru/Ni-MoO_x and Ru-MoO_x. The Gibbs free energy diagrams for the OER pathways on Ru sites in both structures are shown in Fig. 5(d). The rate-determining step (RDS) for both catalysts is the transformation of *OOH from *O. Notably, the adsorption energy barrier (ΔG) of this step is comparatively lower for Ru/Ni-MoO_x (1.65 eV) than for Ru-MoO_x (2.09 eV), indicating a reduced energy barrier and more favorable reaction kinetics on the binary-support catalyst. Additionally, adsorption energy calculations for the Ni sites in Ru/Ni-MoO_x (Fig. S28 in the ESM) demonstrate a higher energy barrier for the RDS compared to the Ru sites, confirming the dominant role of Ru in the catalytic reaction. This result is consistent with previous reports in Refs. [63–65]. We then calculated the adsorption energies at Ru sites for the Ru/Ni-Mo_2N system. The results show that the reconstructed Ru/Ni-MoO_x model exhibits a lower energy barrier for RDS at Ru sites compared to the initial Ru/Ni-Mo_2N (Fig. 5(d) and Fig. S29 in the ESM). This confirms that the surface-reconstructed Ru/Ni-MoO_x model exhibits optimized adsorption behavior at Ru sites, making it a more rational choice for DFT models. To analyze the electronic properties, the projected density of states (PDOS) of Ru 4d orbitals in Ru/Ni-MoO_x and Ru-MoO_x were calculated (Fig. 5(e)). The results show the d-band center of the Ru sites in Ru/Ni-MoO_x is derived as −1.6774 eV, which is lower than that of Ru-MoO_x (−1.3778 eV). Therefore, compared to Ru-Mo_2N, the adsorption of reaction intermediates on the Ru/Ni-MoO_x surface is moderated. This optimized binding strength facilitates the subsequent reaction steps, thereby leading to enhanced OER kinetics. Overall, both experimental and theoretical results collectively demonstrate that anchoring and electronic modulation of Ru sites using a binary support significantly enhance the OER activity of Ru-based catalysts.

2.5 Electrocatalytic overall water splitting performance

The overall water splitting electrolyzer was assembled using Ru/Ni-Mo_2N as the anode and Pt/C as the cathode. This system achieved a cell voltage of 1.483 V at a current density of 10 $mA{\cdot}cm^{-2}$,

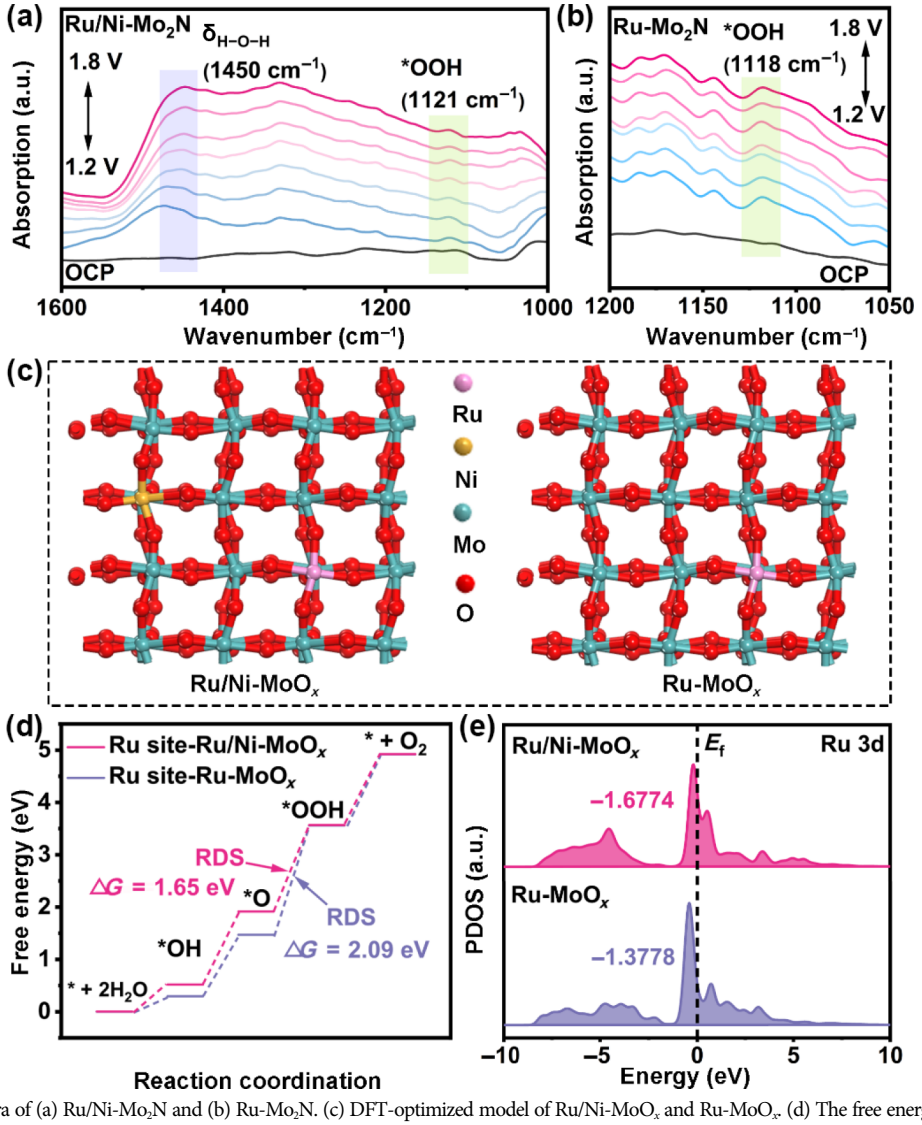

Figure 5 *In-situ* IR spectra of (a) Ru/Ni-Mo_2N and (b) Ru-Mo_2N. (c) DFT-optimized model of Ru/Ni-MoO_x and Ru-MoO_x. (d) The free energy diagram of OER on Ru sites on Ru/Ni-MoO_x and Ru-MoO_x. (e) The PDOS and band centers of Ru 4d orbitals in Ru/Ni-MoO_x and Ru-MoO_x.

outperforming a device assembled with Pt/C||RuO_2 electrodes and those of most reported electrocatalysts (Figs. S30 and S31(b) and Table S5 in the ESM). Long-term stability testing demonstrated stable operation for 230 h at 50 mA·cm^{-2} (Fig. S31(c) in the ESM), confirming the excellent durability. The Faradaic efficiencies (FE) of hydrogen evolution reaction (HER) and OER were calculated to be 99.5% and 98.3%, respectively (Fig. S32(a) in the ESM). During the gas volume measurements, continuous bubbles were observed at the cathode and anode (Fig. S32(b) in the ESM). Gas volume measurements over time revealed an H_2 to O_2 ratio close to 2:1 (Fig. S32(c) in the ESM), consistent with theoretical water electrolysis. We further constructed an AEM electrolyzer using Ru/Ni-Mo_2N as the anode and Pt/C as the cathode (Fig. 6(a)). Performance was evaluated in 1.0 M KOH at temperatures ranging from 30 to 70 °C. Elevated temperature improved ion diffusion and enhanced the reaction kinetics, contributing to higher current densities. Moreover, high temperature may promote the reconstruction of catalyst, further boosting the performance of AEM. At 70 °C, the system required only 1.78 V to reach a current density of 500 mA·cm^{-2} (Fig. 6(b)), outperforming the Pt/C||RuO_2 benchmark (1.97 V) and Pt/C||Ru-Mo_2N (1.94 V) (Figs. S33 and S34 in the ESM). As shown in Figs. 6(c) and 6(d), the Pt/C||Ru/Ni-Mo_2N electrolyzer exhibited operating potentials of 1.57, 1.78, and 1.94 V at current densities of 0.1, 0.5, and 1 A·cm^{-2}, which were lower than those of the Pt/C||RuO_2 system. Furthermore, the AEM electrolyzer showed negligible performance decay during a 517 h continuous operation at 500 mA·cm^{-2} (Fig. 6(e)), demonstrating excellent stability and promising potential for industrial application.

3 Conclusions

In summary, we have demonstrated the promoted role of a binary support (Ni-Mo_2N) on the activity and stability of the Ru sites for OER. The introduction of Ni in the system is helpful to form 3D filamentous network structure with abundant pores, facilitating mass transport. Significantly, the binary Ni-Mo_2N support exhibits a distinct electronic structure compared to Mo_2N, and thus demonstrates superior capability in modulating the electron density of Ru sites. The downshift of the d-band center at Ru sites optimizes the adsorption of reaction intermediates, thereby enhancing the OER activity. Concurrently, the sacrificial behavior of Ni during OER effectively mitigates over-oxidation of Ru and

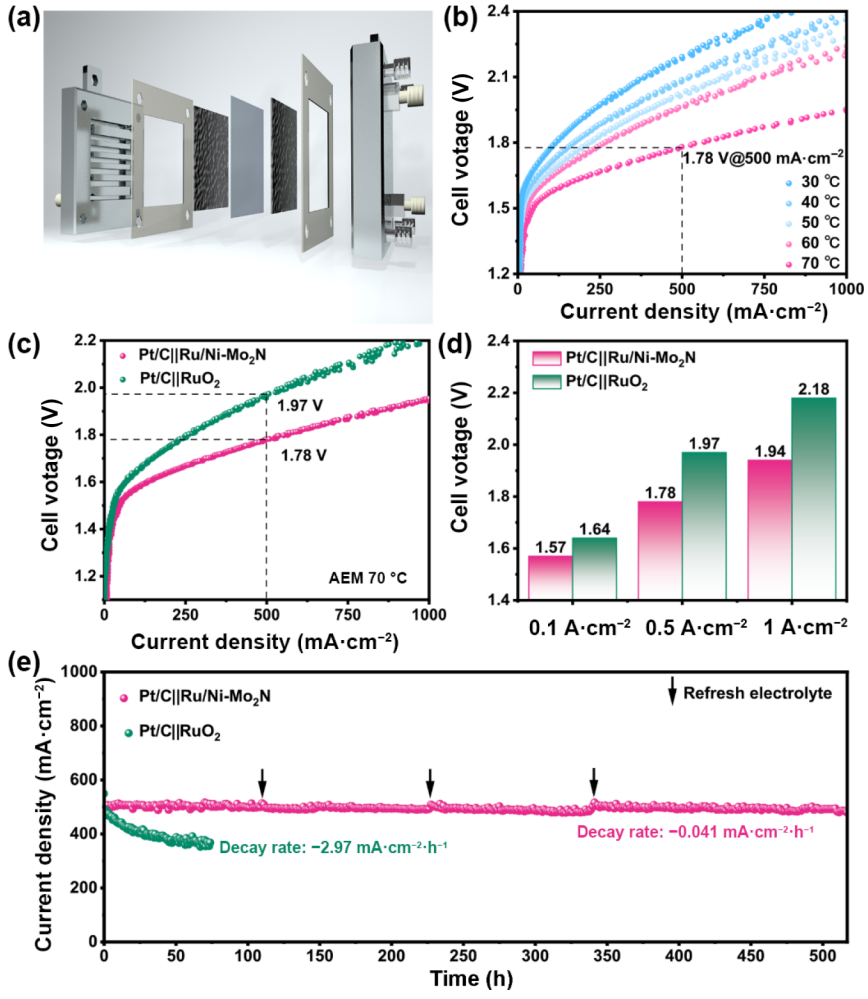

Figure 6 (a) Schematic diagram of the AEMWE device. (b) Polarization curves of Pt/C||Ru/Ni-Mo_2N operating in 1.0 M KOH. (c) Polarization curves compensation of Pt/C||Ru/Ni-Mo_2N and Pt/C||RuO_2. (d) Bar graph of potential at 0.1, 0.5, and 1 A·cm^{-2}. (e) Durability of Pt/C||Ru/Ni-Mo_2N AEMWE assembly at an industrial current density of 500 mA·cm^{-2}.

thereby enhances catalyst stability. The Ru/Ni-Mo_2N catalyst demonstrates good OER performance in 1.0 M KOH, better than Ru-Mo_2N catalyst and most reported Ru-based catalysts. AEMWE of Pt/C||Ru/Ni-Mo_2N (1.78 V@500 mA·cm^{-2}) shows superior performance to Pt/C||RuO_2 (1.97 V@500 mA·cm^{-2}), and can work stably for more than 500 h at 500 mA·cm^{-2}. This work underscores the crucial role of binary support engineering in modulating the electronic structure of Ru, thereby promising the development of low-Ru catalysts for durable water electrolysis technologies.

Electronic Supplementary Material: Supplementary material (electrochemical measurements, experimental details, XRD patterns, SEM images, and theoretical models) is available in the online version of this article at https://doi.org/10.26599/NR.2026.94908372.

Data availability

All data needed to support the conclusions in the paper are presented in the manuscript and the Electronic Supplementary Material. Additional data related to this paper may be requested from the corresponding author upon request.

Acknowledgements

This work was financially supported by the National Natural Science Foundation of China (Nos. 22539002, 91961111, and 22271081) and the Natural Science Foundation of Heilongjiang Province (No. PL2024B017).

Declaration of competing interest

All the contributing authors report no conflict of interests in this work.

Author contribution statement

M. S. X.: Data acquisition, data curation, writing manuscript, experimental design. A. P. W.: Data curation, validation. D. X. W.: Data curation, validation. Y. M. D.: Formal analysis. Y. Y. F.: Formal analysis, methodology. X. Y. Y.: Data analysis. C. G. T.: Project administration, experimental design, writing manuscript. H. G. F.: Project administration, funding acquisition, writing manuscript. All the authors have approved the final manuscript.

Use of AI statement

None.

References

[1] Nairan, A.; Feng, Z.; Zheng, R. M.; Khan, U.; Gao, J. K. Engineering metallic alloy electrode for robust and active water electrocatalysis with large current density exceeding 2000 mA·cm^{-2}. *Adv. Mater.* **2024**, *36*, 2401448.

[2] Cai, Z. X.; Wang, Z. L.; Xia, Y. J.; Lim, H.; Zhou, W.; Taniguchi, A.; Ohtani, M.; Kobiro, K.; Fujita, T.; Yamauchi, Y. Tailored catalytic nanoframes from metal–organic frameworks by anisotropic surface modification and etching for the hydrogen evolution reaction. *Angew. Chem., Int. Ed.* **2021**, *60*, 4747–4755.

[3] Li, J.; Wu, N. T.; Zhang, J.; Wu, H. H.; Pan, K. M.; Wang, Y. X.; Liu, G. L.; Liu, X. M.; Yao, Z. P.; Zhang, Q. B. Machine learning-assisted low-dimensional electrocatalysts design for hydrogen evolution reaction. *Nano-Micro Lett.* **2023**, *15*, 227.

[4] Kang, X.; Yang, F. N.; Zhang, Z. Y.; Liu, H. M.; Ge, S. Y.; Hu, S. Q.; Li, S. H.; Luo, Y. T.; Yu, Q. M.; Liu, Z. B. et al. A corrosion-resistant RuMoNi catalyst for efficient and long-lasting seawater oxidation and anion exchange membrane electrolyzer. *Nat. Commun.* **2023**, *14*, 3607.

[5] Henkensmeier, D.; Cho, W. C.; Jannasch, P.; Stojadinovic, J.; Li, Q. F.; Aili, D.; Jensen, J. O. Separators and membranes for advanced alkaline water electrolysis. *Chem. Rev.* **2024**, *124*, 6393–6443.

[6] Gao, T. Q.; Wang, W. Z.; Zhang, Z. N.; Li, W. Y.; Gao, H. H.; Liu, J. W.; Zhao, X. J.; Liu, Z. H.; Chen, Y. Dual-anion regulation engineering enhances chloridion corrosion resistance for long-lasting industrial-scale seawater splitting. *Chem. Sci.* **2025**, *16*, 15684–15696.

[7] Suen, N. T.; Hung, S. F.; Quan, Q.; Zhang, N.; Xu, Y. J.; Chen, H. M. Electrocatalysis for the oxygen evolution reaction: Recent development and future perspectives. *Chem. Soc. Rev.* **2017**, *46*, 337–365.

[8] Wu, Y. J.; Liu, J. Q.; Li, Q. H.; Zhu, Y.; Li, Q.; Chen, X.; Deng, J. X.; Miao, J.; Cao, Y. L.; Lin, K. et al. Ultrafine ruthenium oxide nanoparticles confined CoNi-MOF via a "ship-in-a-bottle" strategy for efficient oxygen evolution electrocatalysis in alkaline. *Nano Res.* **2025**, *18*, 94907410.

[9] Gao, T. Q.; Zhou, Y. Q.; Zhao, X. J.; Liu, Z. H.; Chen, Y. Borate anion-intercalated NiV-LDH nanoflakes/NiCoP nanowires heterostructures for enhanced oxygen evolution selectivity in seawater splitting. *Adv. Funct. Mater.* **2024**, *34*, 2315949.

[10] Kong, F. Y.; Wu, A. P.; Wang, S. Y.; Zhang, X. H.; Tian, C. G.; Fu, H. G. The "mediated molecular"-assisted construction of Mo_2N islands dispersed on Co-based nanosheets for high-efficient electrocatalytic hydrogen evolution reaction. *Nano Res.* **2023**, *16*, 10857–10866.

[11] Jing, X. Y.; Mu, Y.; Gao, Z. M.; Dong, X. Y.; Meng, C. G.; Huang, C.; Zhang, Y. F. Intermetallic ferric nickel silicide alloy derived from magadiite by magnesiothermic reaction as bifunctional electrocatalyst for overall water splitting. *Nano Res. Energy* **2024**, *3*, e9120104.

[12] Wang, Y. N.; Zhang, M. C.; Kang, Z. Y.; Shi, L.; Shen, Y. C.; Tian, B. Y.; Zou, Y. C.; Chen, H.; Zou, X. X. Nano-metal diborides-supported anode catalyst with strongly coupled TaO_x/IrO_2 catalytic layer for low-iridium-loading proton exchange membrane electrolyzer. *Nat. Commun.* **2023**, *14*, 5119.

[13] Zhang, B.; Zheng, X. L.; Voznyy, O.; Comin, R.; Bajdich, M.; García-Melchor, M.; Han, L. L.; Xu, J. X.; Liu, M.; Zheng, L. R. et al. Homogeneously dispersed multimetal oxygen-evolving catalysts. *Science* **2016**, *352*, 333–337.

[14] Chen, D.; Zhao, H. Y.; Yu, R. H.; Yu, K. S.; Zhu, J. W.; Jiao, J. X.; Mu, X. Q.; Yu, J.; Wu, J. S.; Mu, S. C. Heteroanion induced structural asymmetricity centered on Ru sites switches the rate-determining step of acid water oxidation. *Energy Environ. Sci.* **2024**, *17*, 1885–1893.

[15] Wu, M.; Fan, Y. Y.; Huang, Y.; Wang, D. X.; Xie, Y.; Wu, A. P.; Tian, C. G. Synergistic Ru/RuO_2 heterojunctions stabilized by carbon coating as efficient and stable bifunctional electrocatalysts for acidic overall water splitting. *Nano Res.* **2024**, *17*, 6931–6939.

[16] Liu, H.; Zhang, Z.; Fang, J. J.; Li, M. X.; Sendeku, M. G.; Wang, X.; Wu, H. Y.; Li, Y. P.; Ge, J. J.; Zhuang, Z. B. et al. Eliminating over-oxidation of ruthenium oxides by niobium for highly stable electrocatalytic oxygen evolution in acidic media. *Joule* **2023**, *7*, 558–573.

[17] Yao, Y. C.; Hu, S. L.; Chen, W. X.; Huang, Z. Q.; Wei, W. C.; Yao, T.; Liu, R. R.; Zang, K. T.; Wang, X. Q.; Wu, G. et al. Engineering the electronic structure of single atom Ru sites via compressive strain boosts acidic water oxidation electrocatalysis. *Nat. Catal.* **2019**, *2*, 304–313.

[18] Chang, J. W.; Shi, Y. Y.; Wu, H.; Yu, J. K.; Jing, W.; Wang, S. Y.; Waterhouse, G. I. N.; Tang, Z. Y.; Lu, S. Y. Oxygen radical coupling on short-range ordered Ru atom arrays enables exceptional activity and stability for acidic water oxidation. *J. Am. Chem. Soc.* **2024**, *146*, 12958–12968.

[19] Zhang, J. J.; Busari, F. K.; Zhang, Y. F.; Guo, S.; Zhao, Y.; Wang, B. L.; Zeng, Q.; Zhao, Z.; Li, G. RuO_x clusters anchored on self-assembled SnO_2 cubic nanocage for boosting sustainable acidic water oxidation. *Nano Res. Energy* **2025**, *4*, e9120140.

[20] Tian, C. A.; Liu, R.; Zhang, Y.; Yang, W. X.; Wang, B. Ru-doped functional porous materials for electrocatalytic water splitting. *Nano Res.* **2024**, *17*, 982–1002.

[21] Guo, C. Y.; Shen, L. Y.; Tang, Y. J.; Chen, M. Y.; Zhou, X. X.; Ciucci, F.; Tang, Z. H. Ru single atoms anchored on Co-NC for nitrate electroreduction toward NH_3 synthesis. *Nano Res.* **2025**, *18*, 94907623.

[22] Li, G. K.; Jang, H.; Liu, S. G.; Li, Z. J.; Kim, M. G.; Qin, Q.; Liu, X.; Cho, J. The synergistic effect of Hf–O–Ru bonds and oxygen vacancies in Ru/HfO_2 for enhanced hydrogen evolution. *Nat. Commun.* **2022**, *13*, 1270.

[23] She, S. X.; Chen, C. S.; Fan, K.; Chen, G.; Zhu, Y. P.; Guan, D. Q.; Huang, Y. C.; Chen, H. C.; Lin, Z. Z.; Wong, H. F. et al. Optimizing the Ru catalyst–support interaction via tunnel size of MnO_2 support for enhanced acidic water oxidation. *J. Am. Chem. Soc.* **2025**, *147*, 24392–24402.

[24] Bai, X. F.; Zhang, X. P.; Sun, Y. J.; Huang, M. C.; Fan, J. T.; Xu, S. Y.; Li, H. Low ruthenium content confined on boron carbon nitride as an efficient and stable electrocatalyst for acidic oxygen evolution reaction. *Angew. Chem., Int. Ed.* **2023**, *135*, e202308704.

[25] Zhu, J. W.; Lu, R. H.; Shi, W. J.; Gong, L.; Chen, D.; Wang, P. Y.; Chen, L.; Wu, J. S.; Mu, S. C.; Zhao, Y. Epitaxially grown Ru clusters–nickel nitride heterostructure advances water electrolysis kinetics in alkaline and seawater media. *Energy Environ. Mater.* **2023**, *6*, e12318.

[26] Li, J. Y.; Tan, Y.; Zhang, M. K.; Gou, W. Y.; Zhang, S.; Ma, Y. Y.; Hu, J.; Qu, Y. Q. Boosting electrocatalytic activity of Ru for acidic hydrogen evolution through hydrogen spillover strategy. *ACS Energy Lett.* **2022**, *7*, 1330–1337.

[27] Xu, J. Y.; Liu, T. F.; Li, J. J.; Li, B.; Liu, Y. F.; Zhang, B. S.; Xiong, D. H.; Amorim, I.; Li, W.; Liu, L. F. Boosting the hydrogen evolution performance of ruthenium clusters through synergistic coupling with cobalt phosphide. *Energy Environ. Sci.* **2018**, *11*, 1819–1827.

[28] Wu, Z. X.; Zhao, Y.; Wu, H. B.; Gao, Y. X.; Chen, Z.; Jin, W.; Wang, J. S.; Ma, T. Y.; Wang, L. Corrosion engineering on iron foam toward efficiently electrocatalytic overall water splitting powered by sustainable energy. *Adv. Funct. Mater.* **2021**, *31*, 2010437.

[29] Zhai, P. L.; Xia, M. Y.; Wu, Y. Z.; Zhang, G. H.; Gao, J. F.; Zhang, B.; Cao, S. Y.; Zhang, Y. T.; Li, Z. W.; Fan, Z. Z. et al. Engineering single-atomic ruthenium catalytic sites on defective nickel-iron layered double hydroxide for overall water splitting. *Nat. Commun.* **2021**, *12*, 4587.

[30] Zhao, J. T.; Wang, J.; Yao, J. X.; Li, L.; Chen, D. M.; Li, G.; Zhang,

G. Q. Delicate control over electron distribution and water dissociation kinetics in strongly coupled Ru@NMoC hybrid catalyst realizes efficient seawater electrolysis. *Angew. Chem., Int. Ed.* **2025**, *64*, e202505031.

[31] Li, J.; Wang, X. Y.; Zhu, B. J.; Zhou, Z.; Pan, K. M.; Liu, X. M.; Zhuang, Z. L.; Zhang, Q. B. Recent advances and future prospects of ruthenium phosphide electrocatalysts for the hydrogen evolution reaction. *Rare Met.* **2025**, *44*, 1411–1442.

[32] Kim, M.; Kim, S. H.; Park, J.; Lee, S.; Jang, I.; Kim, S.; Lee, C. Y.; Kwon, O. J.; Ham, H. C.; Hupp, J. T. et al. Reconstructing oxygen-deficient zirconia with ruthenium catalyst on atomic-scale interfaces toward hydrogen production. *Adv. Funct. Mater.* **2023**, *33*, 2300673.

[33] Yuan, C. Z.; Wang, S.; San Hui, K.; Wang, K. X.; Li, J. F.; Gao, H. X.; Zha, C. Y.; Zhang, X. M.; Dinh, D. A.; Wu, X. L. et al. *In-situ* immobilizing atomically dispersed Ru on oxygen-defective Co_3O_4 for efficient oxygen evolution. *ACS Catal.* **2023**, *13*, 2462–2471.

[34] Feng, D.; Wang, P. Y.; Qin, R.; Shi, W. J.; Gong, L.; Zhu, J. W.; Ma, Q. L.; Chen, L.; Yu, J.; Liu, S. L. et al. Flower-like amorphous MoO_{3-x} stabilized Ru single atoms for efficient overall water/seawater splitting. *Adv. Sci.* **2023**, *10*, 2300342.

[35] Zhang, H. M.; Liu, W. H.; Li, Z. H.; Qiao, L.; Chi, K. B.; Guo, X. Y.; Cao, D.; Cheng, D. J. Constructing CoP/Ni_2P heterostructure confined Ru sub-nanoclusters for enhanced water splitting in wide pH conditions. *Adv. Sci.* **2024**, *11*, 2401398.

[36] Niu, Z. Q.; Lu, Z. K.; Qiao, Z. L.; Wang, S. T.; Cao, X. H.; Chen, X. D.; Yun, J.; Zheng, L. R.; Cao, D. P. Robust Ru–VO_2 bifunctional catalysts for all-pH overall water splitting. *Adv. Mater.* **2024**, *36*, 2310690.

[37] Cheng, H. F.; Kamegawa, T.; Mori, K.; Yamashita, H. Surfactant-free nonaqueous synthesis of plasmonic molybdenum oxide nanosheets with enhanced catalytic activity for hydrogen generation from ammonia borane under visible light. *Angew. Chem., Int. Ed.* **2014**, *53*, 2910–2914.

[38] Yu, S. Q.; Xiong, Z.; Zhou, H. T.; Zhang, Q.; Wang, Z. H.; Ma, F.; Qu, Z. H.; Zhao, Y.; Chu, X. B.; Zhang, X. W. et al. Homogenized NiO_x nanoparticles for improved hole transport in inverted perovskite solar cells. *Science* **2023**, *382*, 1399–1404.

[39] Zhao, S. S.; Dang, Q.; Cao, A. Q.; Sendeku, M. G.; Liu, H.; Peng, J.; Fan, Y. M.; Li, H.; Wang, F. M.; Kuang, Y. et al. Hydroxylation strategy enables Ru–Mn oxide for stable proton exchange membrane water electrolysis under 1 $A \cdot cm^{-2}$. *ACS Nano* **2025**, *19*, 8773–8785.

[40] Sun, X. T.; Yu, J. F.; Zada, H.; Han, Y.; Zhang, L.; Chen, H. C.; Yin, W.; Sun, J. Reaction-induced unsaturated Mo oxycarbides afford highly active CO_2 conversion catalysts. *Nat. Chem.* **2024**, *16*, 2044–2053.

[41] Xie, D.; Ding, L. X.; Chen, S. B.; Chen, G. F.; Cheng, H.; Wang, H. H. High mass transfer rate in electrocatalytic hydrogen evolution achieved with efficient quasi-gas phase system. *Angew. Chem., Int. Ed.* **2025**, *137*, e202414493.

[42] Chen, J. H.; Ma, Y. R.; Cheng, C.; Huang, T.; Luo, R. H.; Xu, J. W.; Wang, X. Y.; Jiang, T. L.; Liu, H. X.; Liu, S. et al. Cobalt-doped Ru@RuO_2 core–shell heterostructure for efficient acidic water oxidation in low-Ru-loading proton exchange membrane water electrolyzers. *J. Am. Chem. Soc.* **2025**, *147*, 8720–8731.

[43] Yuan, B. C.; Dang, Q.; Liu, H.; Sendeku, M. G.; Peng, J.; Fan, Y. M.; Cai, L.; Cao, A. Q.; Chen, S. Y.; Li, H. et al. Synergistic niobium and manganese co-doping into RuO_2 nanocrystal enables PEM water splitting under high current. *Nat. Commun.* **2025**, *16*, 4583.

[44] He, W. D.; Tan, X. H.; Guo, Y. Y.; Xiao, Y. H.; Cui, H.; Wang, C. X. Grain-boundary-rich RuO_2 porous nanosheet for efficient and stable acidic water oxidation. *Angew. Chem., Int. Ed.* **2024**, *63*, e202405798.

[45] Liu, T. T.; Guo, H. Y.; Chen, Y.; Zhang, Z. P.; Wang, F. Role of MoO_x surficial modification in enhancing the OER performance of Ru-pyrochlore. *Small* **2023**, *19*, 2206698.

[46] Hou, M. Y.; Zheng, L. R.; Zhao, D.; Tan, X.; Feng, W. Y.; Fu, J. T.; Wei, T. X.; Cao, M. H.; Zhang, J. T.; Chen, C. Microenvironment reconstitution of highly active Ni single atoms on oxygen-incorporated Mo_2C for water splitting. *Nat. Commun.* **2024**, *15*, 1342.

[47] Ge, C.; Li, Z. J.; Chang, Y. N.; Li, T. F.; He, B.; Lu, T. Y.; Xu, L. The manipulation of Ni/MnO heterostructures within carbon hierarchical superstructures as bifunctional oxygen electrocatalysts for enhanced Zn–air batteries. *Rare Met.* **2025**, *44*, 3107–3118.

[48] Su, D. N.; Zhang, X. M.; Wu, A. P.; Yan, H. J.; Liu, Z. Y.; Wang, L.; Tian, C. G.; Fu, H. G. CoO–Mo_2N hollow heterostructure for high-efficiency electrocatalytic hydrogen evolution reaction. *NPG Asia Mater.* **2019**, *11*, 78.

[49] Cai, H. Z.; Yang, H. P.; He, S. Z.; Wan, D.; Kong, Y.; Li, D. L.; Jiang, X. X.; Zhang, X.; Hu, Q.; He, C. X. Size-adjustable high-entropy alloy nanoparticles as an efficient platform for electrocatalysis. *Angew. Chem., Int. Ed.* **2025**, *64*, e202423765.

[50] Chen, Z. J.; Ma, T. Y.; Wei, W.; Wong, W. Y.; Zhao, C.; Ni, B. J. Work function-guided electrocatalyst design. *Adv. Mater.* **2024**, *36*, 2401568.

[51] Wang, Y.; Zhu, Y. L.; Zhao, S. L.; She, S. X.; Zhang, F. F.; Chen, Y.; Williams, T.; Gengenbach, T.; Zu, L. H.; Mao, H. Y. et al. Anion etching for accessing rapid and deep self-reconstruction of precatalysts for water oxidation. *Matter* **2020**, *3*, 2124–2137.

[52] Du, W.; Shi, Y. M.; Zhou, W.; Yu, Y. F.; Zhang, B. Unveiling the *in-situ* dissolution and polymerization of Mo in Ni_4Mo alloy for promoting the hydrogen evolution reaction. *Angew. Chem., Int. Ed.* **2021**, *60*, 7051–7055.

[53] Shao, L.; Han, X. D.; Shi, L.; Wang, T. Z.; Zhang, Y. S.; Jiang, Z. Q.; Yin, Z. X.; Zheng, X. R.; Li, J. H.; Han, X. P. et al. *In-situ* generation of molybdate-modulated nickel-iron oxide electrodes with high corrosion resistance for efficient seawater electrolysis. *Adv. Energy Mater.* **2024**, *14*, 2303261.

[54] Zhang, Q.; Xiao, W.; Shi, J. X.; Lei, J. L.; Xiao, Q.; Luo, H. Q.; Li, N. B. Dynamic molybdate oxyanion boosts self-optimization and self-healing on the NiMoFe heterostructure for water splitting in alkaline media. *ACS Catal.* **2024**, *14*, 18003–18017.

[55] Fan, Y. Y.; Li, Z. H.; Liu, Y.; Liu, J. N.; Wang, D. X.; Yan, H. J.; Gubanov, A. I.; Wu, A. P.; Tian, C. G. Nickel-based hollow spheres with optimized interfacial electronic structures by highly dispersed MoN for efficient urea electrolysis. *Adv. Funct. Mater.* **2025**, *35*, 2421222.

[56] Chen, Y. Y.; Zhang, Y.; Zhang, X.; Tang, T.; Luo, H.; Niu, S.; Dai, Z. H.; Wan, L. J.; Hu, J. S. Self-templated fabrication of $MoNi_4/MoO_{3-X}$ nanorod arrays with dual active components for highly efficient hydrogen evolution. *Adv. Mater.* **2017**, *29*, 1703311.

[57] Zhang, H. G.; Yohannes, A.; Zhao, H.; Li, Z.; Xiao, Y. J.; Cheng, X.; Wang, H.; Li, Z. K.; Siahrostami, S.; Kibria, M. G. et al. Photocatalytic asymmetric C–C coupling for CO_2 reduction on dynamically reconstructed $Ru^{\delta+}$–O/Ru^0–O sites. *Nat. Commun.* **2025**, *16*, 534.

[58] Zhou, Y. F.; Mao, Y.; Ye, C. Z.; Wang, Z. Y.; Wei, S. H.; Kennedy, J. V.; Zhao, Y. F.; Yang, H.; Cowie, B. C. C.; Waterhouse, G. I. N. Ru single atoms anchored on Co_3O_4 nanorods for efficient overall water splitting under pH-universal conditions. *Adv. Energy Mater.* **2025**, *15*, 2500700.

[59] Duan, X. X.; Wen, N.; Liu, S.; Li, H. P.; Jiao, X. L.; Chen, D. R.; Xia, Y. G. Lattice strain engineering in Ru-based electrocatalysts for efficient acidic overall water splitting and Ru dissolution suppression. *ACS Catal.* **2025**, *15*, 10119–10129.

[60] Sun, J. P.; Zhou, S.; Zhao, Z.; Qin, S. Y.; Meng, X. C.; Tung, C. H.; Wu, L. Z. Deep reconstruction of a Mo-based electrocatalyst for high-performance water/seawater oxidation at Ampere-level current density. *Energy Environ. Sci.* **2025**, *18*, 1952–1962.

[61] Sun, J. P.; Ren, G. M.; Qin, S. Y.; Zhao, Z.; Li, Z. Z.; Zhang, Z. S.; Li,

C. H.; Meng, X. C. Reconstruction Co–O–Mo in amorphous-crystalline MoO_x/$Co(OH)_2$ interface for industry-level active and stable electrocatalytic seawater hydrogen evolution. *Nano Energy* **2024**, *121*, 109246.

[62] Ma, S. Y.; Wang, Z. H.; Liu, B. W.; Wang, X. L.; Du, S. C.; Song, Z. C.; Bian, X. X.; Hao, M. C.; Huang, J.; Chen, Z. M. et al. Interface-induced enhancement of paired electrolysis in 5-hydroxymethylfurfural–H_2O system on symbiotic nickel/molybdenum nitride heterostructure. *Chem. Eng. J.* **2023**, *476*, 146490.

[63] Liu, R.; Sun, M. Z.; Liu, X. J.; Lv, Z. H.; Yu, X. Y.; Wang, J. M.; Liu, Y. R.; Li, L. H.; Feng, X.; Yang, W. X. et al. Enhanced metal–support interactions boost the electrocatalytic water splitting of supported ruthenium nanoparticles on a Ni_3N/NiO heterojunction at industrial current density. *Angew. Chem., Int. Ed.* **2023**, *62*, e202312644.

[64] Li, C. Q.; Kim, B.; Li, Z. P.; Thapa, R.; Zhang, Y. F.; Seo, J. M.; Guan, R. N.; Tang, F.; Baek, J. H.; Kim, Y. H. et al. Direct Electroplating ruthenium precursor on the surface oxidized nickel foam for efficient and stable bifunctional alkaline water electrolysis. *Adv. Mater.* **2024**, *36*, 2403151.

[65] Yang, W. W.; Wang, Z. J.; Zhang, J.; Jia, L. Y.; Li, J. H.; Chen, X. Y.; Liu, X. Y.; Zhang, H. Y.; Lin, J. K.; Zhao, M. et al. Interfacial engineering and structural modulation of RuO_2-based catalysts for highly active and durable oxygen evolution reaction in acidic environment. *Angew. Chem., Int. Ed.* **2025**, *64*, e202509768.